IOP Publishing *Quantum Sci. Technol.* **10** (2025) 045076 https://doi.org/10.1088/2058-9565/ae1161

Quantum Science and Technology

OPEN ACCESS

RECEIVED
18 July 2025

REVISED
8 September 2025

ACCEPTED FOR PUBLICATION
9 October 2025

PUBLISHED
28 October 2025

PAPER

Transportable strontium lattice clock with 4×10^{-19} blackbody radiation shift uncertainty

I Nosske*, C Vishwakarma, T Lücke, J Rahm, N Poudel, S Weyers, E Benkler,
S Dörscher and C Lisdat*

Physikalisch-Technische Bundesanstalt, Bundesallee 100, 38116 Braunschweig, Germany
* Authors to whom any correspondence should be addressed.

E-mail: ingo.nosske@ptb.de and christian.lisdat@ptb.de

Keywords: transportable optical clock, optical lattice clock, strontium atoms, blackbody radiation shift, single-beam magneto-optical trap, absolute frequency

Abstract

We describe a transportable optical lattice clock based on the $^1S_0 \rightarrow {}^3P_0$ transition of lattice-trapped ^{87}Sr atoms with a total systematic uncertainty of 2.1×10^{-18}. The blackbody radiation shift, which is the leading systematic effect in many strontium lattice clocks, is controlled at the level of 4.0×10^{-19}, as the atoms are interrogated inside a well-characterised, cold thermal shield. Using a transportable clock laser, the clock reaches a frequency instability of about $5 \times 10^{-16}/\sqrt{\tau/\mathrm{s}}$, which enables fast reevaluations of systematic effects. By comparing this clock to the primary caesium fountain clocks CSF1 and CSF2 at Physikalisch-Technische Bundesanstalt, we measure the clock transition frequency with a fractional uncertainty of 1.9×10^{-16}, in agreement with previous results. The clock was successfully transported and operated at different locations. It holds the potential to be used for geodetic measurements with centimetre-level or better height resolution and for accurate inter-institute frequency comparisons.

1. Introduction

State-of-the-art optical atomic clocks have reached fractional systematic uncertainties of few 10^{-18} and below [1–9]. This progress in the field of optical frequency metrology has triggered active discussions of the redefinition of the SI second [10]. One of the mandatory criteria for such a redefinition is the validation of optical clocks by inter-institute comparisons [10, 11]. A transportable optical clock can be used as a frequency reference for achieving this goal. Another field that benefits from the development of highly accurate transportable clocks is chronometric geodesy [12], which can rival the uncertainties of geopotentials determined by state-of-the-art geodetic techniques, typically equivalent to a few centimetres of physical height [13]. This will facilitate improved and more consistent height reference systems and allow for better Earth monitoring. These and other applications, however, require transportable clocks with performance comparable to the best laboratory-based systems. Several groups are developing transportable optical clocks [14–23], but few have reached similar performance as the best laboratory-based clocks [17, 23].

Here, we present our second-generation transportable strontium optical lattice clock Sr4 that was already used in off-site measurements [11]. Several fundamental design changes improved the performance compared to its predecessor Sr2 [14]: the uncertainty of the blackbody radiation (BBR) shift, often representing the largest uncertainty contribution in optical lattice clocks [2, 6, 24–26], is reduced to 4.0×10^{-19} by transporting the atoms into a cooled copper shield for interrogation, inspired by a design from RIKEN [27]. This represents an improvement of a factor of about 2 compared to the lowest BBR shift uncertainties reached in strontium lattice clocks [6, 9, 27, 28], and more than an order of magnitude improvement compared to our previous transportable clock [14]. Unlike the approach in [29], it does not require moving mechanical parts. A new transportable clock laser [30] allows for a clock instability of about $5 \times 10^{-16}/\sqrt{\tau/\mathrm{s}}$, which reduces the averaging time τ required for reevaluations of

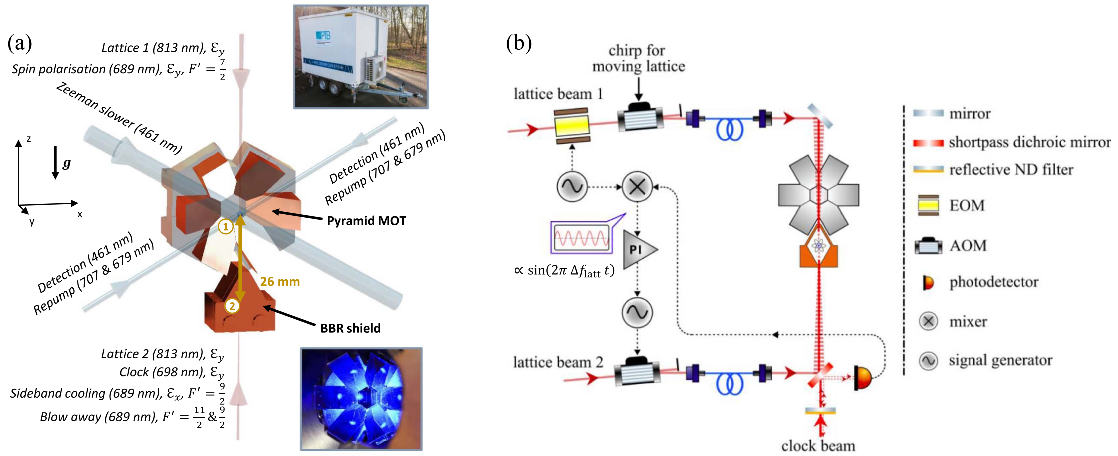

Figure 1. Layout of the core components of the physics package. (a) A model of the pyramid MOT (1) and the BBR shield (2) in the centre of the main vacuum chamber, together with all laser beams except the MOT cooling beam. For the vertical beams the linear polarisation direction is indicated, where this is relevant. The upper state hyperfine levels of ^{87}Sr addressed by the 689 nm beams are also given. The upper inset shows the air-conditioned car trailer of the clock. In the lower inset, the central fluorescence of strontium atoms as well as reflections from the mirrors during the first-stage MOT can be seen. (b) Optics setup which subsequently enables a moving lattice and Doppler cancellation of the lattice and clock beams, similar to [27]. The relative phase of the two lattice beams is stabilised while the atoms are in the BBR shield. The reflective neutral density (ND) filter serves as end reference surface for the path length stabilisation of the 698 nm clock light and thus ensures that no Doppler shift between the lattice-trapped atoms and the clock laser beam occurs. For details see text.

systematic effects by more than one order of magnitude compared to our previous configuration [14, 31]. The estimated total systematic uncertainty of the clock is 2.1×10^{-18}, which is in the range of state-of-the-art laboratory systems and represents a significant step towards enabling the applications outlined above. We determine the ^{87}Sr clock transition's absolute frequency by comparison to the primary caesium fountain clocks CSF1 and CSF2 at Physikalisch-Technische Bundesanstalt (PTB) [32].

2. Clock setup

The physics package for laser cooling and trapping the strontium atoms, the required lasers and the electronic drivers are mounted in an air-conditioned car trailer (see [14] for details). The trailer also houses a frequency comb that allows to measure the frequency ratio between the fundamental wavelength of the clock laser at 1397 nm [30] and light from the long-distance interferometric fibre links in Europe at 1542 nm [33, 34]. The ratio is measured in a single branch of the comb without uncompensated optical paths [35]. The comb has an additional branch at 813 nm to measure the lattice laser wavelength. The mass of all components inside the trailer is about 700 kg.

The ultra-high vacuum system for trapping and interrogation of ^{87}Sr atoms is pumped by non-evaporable getter and ion getter pumps. The latter can be switched off for more than one week without a lasting vacuum degradation. A strontium beam is generated in an oven by heating metal to about 500 °C. A level scheme with the relevant electronic transitions in ^{87}Sr is shown in appendix A. The atoms are decelerated in a permanent magnet transverse field Zeeman slower operating on the $^1S_0 \rightarrow {}^1P_1$ (461 nm) transition [36]. The atoms are trapped 33 cm downstream from the oven nozzle in a single 5 cm-diameter ($1/e^2$) beam on the $^1S_0 \rightarrow {}^1P_1$ transition in a pyramid MOT [37], which consists of six silver-coated mirrors made from oxygen-free copper and a central sharp-edged CaF$_2$ prism mounted in the vacuum chamber, see figure 1(a). The copper substrates are screwed to an aluminium base plate; the CaF$_2$ prism is held by glue and secured by clamp. Optical access for additional laser beams, as well as the atomic beam, is granted by cusps between the six mirror elements.

A water-cooled anti-Helmholtz coil pair generates the MOT magnetic field gradients. Three orthogonal Helmholtz coil pairs provide precise magnetic field compensation and control. The centre of the physics package is enclosed by a single-layer 1.5 mm-thick μ-metal shield. Despite having holes for the required laser beams, cables and vacuum system connections, the μ-metal shield provides a magnetic shielding factor at its centre of $\gtrsim 100$, which enables re-trapping of atoms in the optical lattice without the need for new field compensation after transporting the clock to another site.

During a second-stage laser cooling of ^{87}Sr atoms to a few μK via the $^1S_0 \rightarrow {}^3P_1$ (689 nm) transition [38], the atoms are loaded into an optical lattice formed by two counter-propagating beams at 813 nm. The lattice is operated close to the $E1$ magic frequency for the clock transition. Below the pyramid MOT

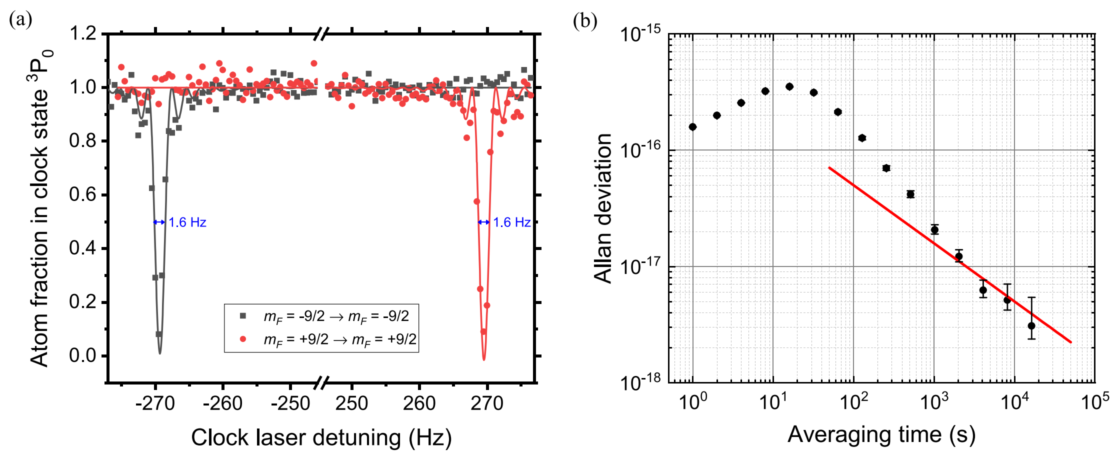

Figure 2. Spectroscopy of and stabilisation on the 698 nm clock transition. (a) Scans of the clock transition of atomic samples spin-polarised in the $m_F = \pm 9/2$ states with 500 ms Rabi interrogation pulses. The solid lines are fits with the expected line shape. (b) Frequency stability of a comparison between the transportable lattice clock Sr4 and the laboratory clock Sr3 [39], which is much more stable thanks to an ultra-stable silicon resonator [40]. The line indicates the Sr4 instability of $5 \times 10^{-16}/\sqrt{\tau/\mathrm{s}}$. For this measurement in Sr4 a dead time of 1192 ms and a Rabi time of 450 ms were used.

assembly, a BBR shield [27] is installed through which the lattice is transmitted via two holes with diameters of about 1 mm. Atoms are moved downwards into the centre of the 20 mm-long copper shield by a frequency chirp on one of the lattice beams. The shield is attached to a pulse tube refrigerator and can be cooled to below 100 K. It not only provides a well-controlled thermal environment with reduced BBR, but also shields the atoms from potentially existing stray electric fields, and from the hot atomic beam and BBR from the oven.

The clock laser with its reference resonator [30] is located outside the trailer in a protected place to avoid vibrations from the air conditioning system and water chillers in the trailer. Its ultra-stable light at 1397 nm is delivered to the physics package via fibre with noise cancellation. There, it is frequency converted in a fibre-to-free-space periodically-poled lithium niobate (PPLN) waveguide frequency doubler to the interrogation wavelength of 698 nm. The endpoint of the fibre noise cancellation at 1397 nm thereby serves as reference point for an optical path length stabilisation of the switched light distribution to the atoms at 698 nm (see figure S4(b)) in [30]).

The clock laser beam to interrogate the $^1S_0 \rightarrow {}^3P_0$ transition is overlapped with the lattice and focussed (like the lattice beams) at the BBR shield centre. The $1/e^2$ beam waists are 110 μm and 66 μm, respectively. Furthermore, laser beams at 689 nm are superimposed with the lattice for axial sideband cooling, spin polarisation and removal of atoms in unwanted states. Where relevant, the polarisations of the beams are indicated in figure 1(a). A magnetic field is applied with varying strength along the y direction during the following steps.

Atoms are moved into the centre of the BBR shield in a 60 ms long transfer phase. The frequency of lattice beam 1 is detuned by at maximum 1.6 MHz with respect to lattice beam 2 to form a moving lattice that shifts the atoms by 26 mm. During the preparation and spectroscopy stages inside the BBR shield, the relative phase of the two lattice beams is stabilised by an acousto-optic modulator (AOM). An electro-optic modulator (EOM) imprints sidebands to generate a Pound-Drever-Hall like error signal, see figure 1(b) for details. In the BBR shield, the atoms are axially sideband cooled and pumped to the $m_F = \pm 9/2$ stretched hyperfine ground-state. To prepare a pure spin sample, atoms in either of the two stretched m_F states are transferred to the $^3P_0$ state by a 60 ms long π pulse on the clock transition. This is done in a bias magnetic field of about 0.41 mT that splits the $m_F = \pm 9/2$, $\Delta m_F = 0$ clock transitions by 4.0 kHz. Remaining ground-state atoms are blown away by an intense beam on the 689 nm transition. After adiabatically reducing the lattice depth to the desired value (typically $15 \ldots 50\,E_{\mathrm{rec}}$ with $E_{\mathrm{rec}} = h \times 3.47$ kHz the recoil energy of a lattice beam photon), we perform Rabi spectroscopy by a typically 500 ms long π pulse on the clock transition at a Zeeman splitting of about 540 Hz.

After the clock interrogation, the atoms are moved back up to the MOT position. Here, the atoms in the $^1S_0$ state are removed from the trap by radiation pressure. The arising 461 nm fluorescence is collected by a photomultiplier tube via a 3$''$ diameter off-axis parabolic mirror, which has a central 35 mm diameter hole along the focal axis to give optical access for the MOT cooling beams. Following the repumping of the remaining atoms from the $^3P_0$ to the $^1S_0$ state, the same detection procedure is

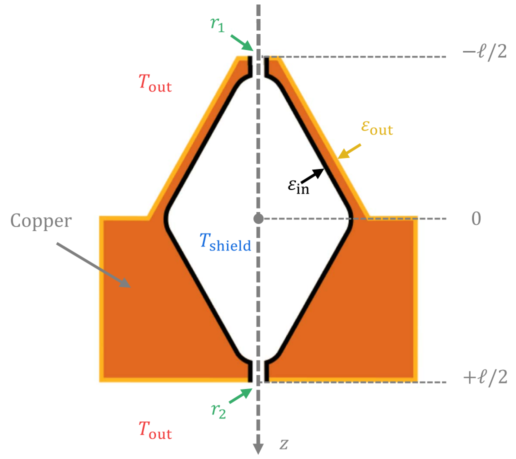

Figure 3. Cut through the BBR shield in the xz plane with indications of the hole positions, hole radii, temperatures and emissivities that are relevant for the BBR shift determination.

repeated. The signal background is recorded in a third detection. The excitation probability is determined from the three signals. Frequency scans over the clock transition are shown in figure 2(a).

For stabilising the clock laser frequency to the atomic resonance, we subsequently interrogate the $m_F = \pm 9/2$ transitions at the low and high frequency half width points. From the four observed excitation probabilities, we estimate the frequency offset of the clock laser from the atomic resonance and the line splitting induced by the magnetic field. By observing the temporal development of the frequency corrections applied to the clock laser, we also estimate the drift rate of the clock laser resonator. To minimise lock errors, we apply a feed forward compensation of the cavity drift [41].

Using the transportable clock laser [30], the clock achieves an instability of $5 \times 10^{-16}/\sqrt{\tau/\mathrm{s}}$, see figure 2(b). For evaluations of systematic frequency shifts in the clock, we interleave two clock stabilisations with different clock parameters, e.g. different lattice trap depths or atom numbers [42]. Here, we observe an asymptotic instability of about $7 \times 10^{-16}/\sqrt{\tau/\mathrm{s}}$, enabling fast characterisations of systematic effects with small statistical measurement uncertainties.

3. BBR shield and shift

The BBR shift often causes the largest uncertainty contribution in state-of-the-art optical lattice clocks [2, 6, 24–26] and therefore requires special attention. Critical parameters are the representative temperature T of the environment and the atomic response to the BBR field. In the electric dipole ($E1$) approximation, the BBR shift $\Delta\nu_{\mathrm{BBR}}(T)$ is often described by the sum of the so-called static contribution $\Delta\nu^{(\mathrm{stat})}(T) \propto T^4$ [43] and the dynamic contribution $\Delta\nu^{(\mathrm{dyn})}(T)$. Here, we express the latter as $\Delta\nu^{(\mathrm{dyn})}(T) = \Delta\nu^{(\mathrm{dyn})}(T_0)\,(T/T_0)^6 f(T/T_0)$ with

$$f(T/T_0) = \frac{\eta_6 + \eta_8\,(T/T_0)^2 + \eta_{10}\,(T/T_0)^4}{\eta_6 + \eta_8 + \eta_{10}} \tag{1}$$

to reproduce the dynamic contribution at $T = T_0 \equiv 300\,\mathrm{K}$ and facilitate computing the uncertainty. We update the coefficients η_i from [44] by scaling them with the fractional difference with respect to the recently reevaluated value $\Delta\nu^{(\mathrm{dyn})}(300\,\mathrm{K}) = -153.06(33)\,\mathrm{mHz}$ [6], where the number in parentheses is the uncertainty referred to the corresponding last digits of the result. The such determined coefficients are $\eta_6 = -0.132\,16\,\mathrm{Hz}$, $\eta_8 = -0.012\,31\,\mathrm{Hz}$ and $\eta_{10} = -0.008\,58\,\mathrm{Hz}$ and agree with the full calculation in [6] within 1×10^{-19} for $T \leqslant 300\,\mathrm{K}$ [45]. The $M1$ BBR shift only amounts to 5.6×10^{-20} at $300\,\mathrm{K}$ [46, 47] and is neglected in the following analysis.

During interrogation, the atoms are mainly exposed to the BBR from the shield at temperature T_{shield}. However, BBR from the outside T_{out} enters through the holes in the shield and may illuminate the atoms directly or after scattering from the walls. The solid angle Ω under which the atoms see the exterior determines the amount of direct line-of-sight room temperature BBR the atoms are exposed to. It depends on the distance between atoms and holes, $z \pm \frac{\ell}{2}$, that is given by the atomic position z with respect to the centre of the shield at $z = 0$ and the length of the BBR shield ℓ (figure 3). For hole radii r_i,

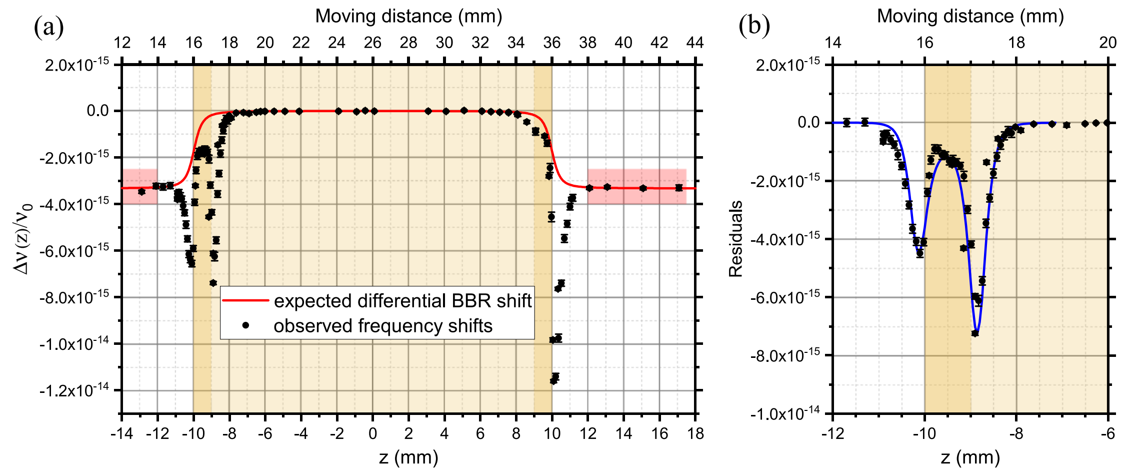

Figure 4. Differential frequency shifts in and around the BBR shield. (a) Position dependent fractional frequency shift relative to the centre of the BBR shield at $T_{\text{shield}} = -50\,^{\circ}\text{C}$ and $T_{\text{out}} = 21\,^{\circ}\text{C}$ (dots), measured by comparing interleaved stabilisations within the transportable clock. The red curve is the expected differential BBR shift according to (4). The light-yellow region denotes the BBR shield interior, the dark-yellow regions its two 1 mm-deep holes. The red regions outside the BBR shield indicate the data points that were used to calculate the experimentally observed differential BBR shift, see text. (b) Residuals between expected BBR and observed frequency shifts (dots). The blue line is a simulation of Stark shifts due to surface potentials.

the fractional solid angle is given by:

$$\frac{\Omega(z)}{4\pi} = \frac{1}{2}\left[1 - \sin\left(\arctan\left(\frac{z+\frac{\ell}{2}}{r_1}\right)\right)\right] + \frac{1}{2}\left[1 + \sin\left(\arctan\left(\frac{z-\frac{\ell}{2}}{r_2}\right)\right)\right] \tag{2}$$

To determine the contribution of the room temperature BBR, the radii of both holes were accurately measured to be 0.484(6) mm (appendix B), resulting in a solid angle of $4\pi \cdot 1.17(3) \times 10^{-3}$ at the BBR shield centre.

The inside of the BBR shield is coated by a high-emissivity coating (Ultra Black$^{\text{TM}}$ by Acktar). Its emissivity for the entire BBR spectrum at room temperature is estimated to be $\epsilon_{\text{in}} = 0.926(43)$ (appendix C). Hence, also BBR from the outside that is scattered on the inner walls may interact with the atoms. This increases the effective solid angle under which the atoms see the holes to [48, 49]

$$\frac{\Omega_{\text{eff}}(z)}{4\pi} = \frac{1}{1 + \left(\frac{4\pi}{\Omega(z)} - 1\right)\epsilon_{\text{in}}}. \tag{3}$$

The position-dependent BBR shift in the shield $\Delta\nu_{\text{BBR}}^{\text{shield}}$ is expected to be:

$$\Delta\nu_{\text{BBR}}^{\text{shield}}(z) = \Delta\nu_{\text{BBR}}(T_{\text{shield}})\left(1 - \frac{\Omega_{\text{eff}}(z)}{4\pi}\right) + \frac{\Omega_{\text{eff}}(z)}{4\pi}\Delta\nu_{\text{BBR}}(T_{\text{out}}) \tag{4}$$

In order to calibrate the position of the atoms in the BBR shield and verify the model in (4), we interleave clock stabilisations with the atoms residing either at $z = 0$ mm or at another distance z in or around the BBR shield. The measured fractional frequency differences are plotted in figure 4 for $T_{\text{shield}} = -50.1(1)\,^{\circ}\text{C}$ and $T_{\text{out}} = 21(1)\,^{\circ}\text{C}$. The error bars are given by the statistics of the measurements. Since the bias magnetic field varies over the probed region, we have corrected the measured shifts for the difference of the second-order Zeeman shifts (section 4.3), which amount to at most 1.7×10^{-17}. In order to check for differential lattice light shifts, we compared the clock frequency at two lattice intensities ($I_2/I_1 = 1.6$) at the centre and inside the upper hole of the BBR shield. As they are measured to be zero-compatible within their statistical measurement uncertainties of $<2 \times 10^{-17}$, they are not included in this analysis. Other effects have been neglected.

The difference of frequency shifts for atoms inside and outside the BBR shield matches the expectations for the BBR shift from (4). The weighted average of the data points for atoms outside the BBR shield and at least 2 mm away from the nearest outer hole edge (see the red-shaded regions in figure 4(a)) is $-3.33(3) \times 10^{-15}$, which agrees with the expected differential BBR shift $\Delta\nu_{\text{BBR}}^{\text{shield}}(|z| > \ell/2 + 2\,\text{mm}) - \Delta\nu_{\text{BBR}}^{\text{shield}}(0) = -3.32(7) \times 10^{-15}$. The uncertainty of the latter value results

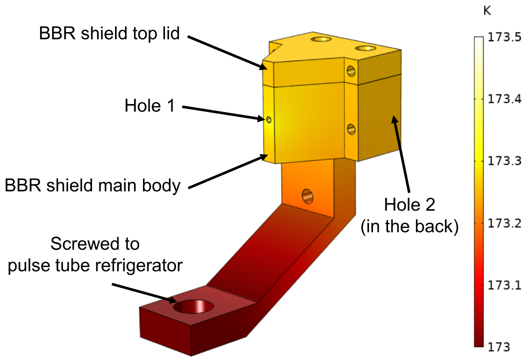

Figure 5. FEM simulation of the temperature of the BBR shield.

from the uncertainty of T_{out}. We neglect the influence of BBR from the outer shield surfaces, as they are polished and have a small emissivity $\epsilon_{\mathrm{out}} \approx 0.03$.

In contrast to the expected smooth development of the shift from the inside to the outside of the BBR shield, we observe localised peaks at the inner and outer edges of the holes. As the cause for the peaks at the outer edges, we consider surface potentials due to the transition from coating to polished copper on the outside of the shield. For a sufficiently thick coating, no further shifts due to differences in the work function on the inner surface would be expected. This behaviour is mostly observed for the hole at $z > 0$ and can be well reproduced by a finite element method (FEM) simulation that incorporates a small varying surface potential on the inner edge of the bore caused by a reduced coating thickness. However, for $z < 0$ much stronger shifts are observed on the inside of the hole. These can be modelled if a linear variation of the surface potential along the bore and an offset from the hole axis are assumed, see figure 4(b). We suspect that the coating in this bore has not reached its intended thickness as in the other, easier to cover regions of the BBR shield, and causes these patch potentials.

For distances to the hole edge Δz large compared to the bore radius r, the shift rapidly falls off with an approximate $\propto \Delta z^{-4}$ scaling. According to fits of the data (see appendix D), the combined residual shift from the two inner hole edges at the BBR shield centre is up to about -1×10^{-19}.

We expect temperature inhomogeneities of the BBR shield due to residual absorption of room temperature BBR and absorption of lattice light near the bores. The latter is apparent due to an increase of the shield temperature by 100 mK when the lattice is turned on and is attributed to suboptimal alignment. In order to assess these effects, we perform a FEM simulation of the actual geometry of the copper BBR shield, including a slightly reduced thermal conductivity between the main body and the top lid, which is cold-welded to the bottom with a 100 μm thick indium foil. The temperature at the bottom of the BBR shield is fixed.

Due to heat intake from the room temperature environment, a cooled BBR shield ($T_{\mathrm{shield}} < T_{\mathrm{out}}$) is slightly warmer at its top than at its bottom. According to the simulation the maximum temperature difference is 11.4 mK for our geometry. To account for the heating by the lattice laser, we adjust the absorbed power to match the observed temperature increase of the shield. The observed heating is consistent with the absorption of about 1% of the lattice beam power. The result of the simulation is shown in figure 5.

We see that the two points where part of the lattice beams are partially absorbed exhibit a temperature increase by about 0.5 K above the BBR shield temperature measured at the Pt100 positions. As this temperature steeply falls off on a length scale of a few 100 μm, it only leads to a negligible atomic BBR shift change of $<1 \times 10^{-19}$ even at room temperature (and less for lower temperatures), if compared to a homogeneous temperature environment. However, the laser heating also leads to smaller temperature gradients on larger length scales in the BBR shield. According to the simulation, we estimate the difference between the warmest and the coldest point of the BBR shield—after removing the warm regions around the lattice beam absorption spots—to be 53 mK (between room temperature and at $-100\,^\circ$C), which is considerably larger than the thermal inhomogeneity caused by room temperature BBR absorption alone. Assuming a rectangular probability distribution of the true temperature value in this range [50], we arrive at a standard uncertainty of 15 mK.

In combination with a calibration uncertainty of the Pt100 sensors, which are mounted at the sides of the shield, of 12.5 mK and a 4 mK uncertainty associated with the measurement bridge, we find an

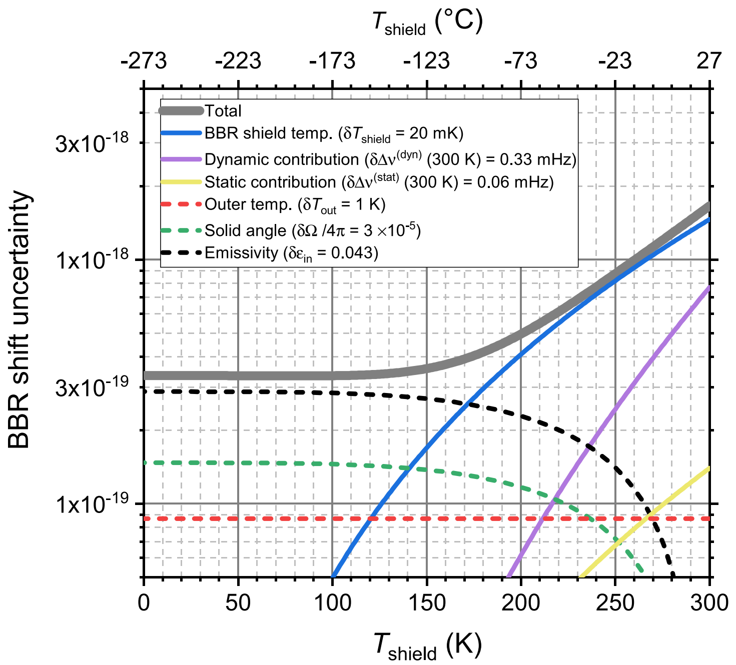

Figure 6. BBR shift uncertainty contributions associated with uncertainties of different quantities versus T_{shield}. The solid (dashed) lines denote uncertainties related to the BBR shift from T_{shield} (T_{out}).

uncertainty of 20 mK for T_{shield} in the range between room temperature and $-100\,^\circ$C. We correct the measured temperatures for the small difference between the thermodynamic temperature and the ITS-90 temperature scale, $T - T_{90}$ [51], which e.g. for 223 K corresponds to $-3.2(2)$ mK and for 173 K to $-6.6(3)$ mK.

The BBR shift uncertainty contributions associated with uncertainties of the parameters T_{shield}, $\Delta\nu^{(\text{dyn})}$, $\Delta\nu^{(\text{stat})}$, T_{out}, $\frac{\Omega}{4\pi}$ and ϵ_{in} are determined by error propagation. In figure 6, they are plotted versus T_{shield}. We note that, as T_{shield} approaches T_{out}, the BBR spectra inside and outside the BBR shield become similar, and hence the uncertainty contributions from $\frac{\Omega}{4\pi}$ and ϵ_{in} decrease. Between room temperature and $-100\,^\circ$C, the uncertainty associated with T_{shield} dominates, while for lower temperatures the uncertainty associated with ϵ_{in} dominates. We operated the clock at $-100\,^\circ$C, where the total BBR shift uncertainty is 4.0×10^{-19}. An increase by slow variations of T_{shield} is avoided by the application of time-resolved corrections of the BBR shift. Compared to [27], the BBR shift uncertainty was roughly halved mainly by a better-known solid angle to the outer environment.

We note that a reduction of the total BBR shift uncertainty to the 10^{-20} regime appears to be feasible with this design type. This would be achievable by, for example, doubling the BBR shield length to 40 mm and for $T_{\text{shield}} \lesssim 100$ K—provided that the uncertainty of the BBR shield temperature does not increase. The corresponding additional moving lattice distance of 10 mm would only result in an additional dead time of $\sim$ 30 ms in our system, only marginally affecting its instability by the Dick effect [52].

4. Other systematic effects

4.1. Density shift

In order to measure the density shift, i.e. interactions between the lattice-trapped fermionic ^{87}Sr atoms during clock spectroscopy, we perform a self-comparison of the clock at interleaved different atom numbers. During this measurement the lattice trap depth is held at $34(3)\,E_{\text{rec}}$. The atom number in one of the two clock operation modes is reduced by shortening the preparation pulse which transfers the atoms in the desired m_F level of the ^{3}P$_0$ state before the actual clock interrogation. In order to evaluate the shift at a different atom number N and lattice depth U, we use the density shift scaling $\propto N U^{3/4}$ [53]. At our typical atom number and at the lattice depth $16(2)\,E_{\text{rec}}$, the resulting density shift is $+0.1(4) \times 10^{-18}$. Its uncertainty is dominated by the statistical uncertainty of the underlying measurement and includes a smaller contribution due to atom number variations during clock operation of up to 50%.

4.2. Lattice light shift

The lattice beams are derived from a titanium:sapphire laser and spectrally filtered by a volume Bragg grating filter with a 23 GHz bandwidth. In order to evaluate the lattice light shift, we perform a clock self-comparison at interleaved lattice depths of $16(2)\,E_{\mathrm{rec}}$ and $35(4)\,E_{\mathrm{rec}}$ at a lattice frequency close to the $E1$ magic frequency [54]. Presently, the frequency stability of the lattice laser is provided by a reference cavity. To ensure better reproducibility after transportation, we will lock the lattice laser to the Sr clock laser via the optical frequency comb. With the lattice light shift model outlined in [55] and the values for the differential $E1$ polarisability and the hyperpolarisability from [54], we calculate a lattice light shift of $+7.4(1.7)\times 10^{-18}$ for the stabilisation cycle with the shallow lattice depth. For the $E2$-$M1$ polarisability coefficient, we use the weighted mean $\tilde{\alpha}^{qm}/h = -1.07(14)\,\mathrm{mHz}$ of the coefficients published in [54] and [56]. The population distribution required as input to the light shift model is determined by sideband spectroscopy. For the shallow [deep] lattice, the fraction of atoms in axial states $n_z > 0$ is 0.16(5) [0.08(5)], the radial temperature is 1.0(5) μK [1.5(5) μK]. The small density shift difference between the two stabilisation cycles is neglected in this analysis.

4.3. Second-order Zeeman shift

The second-order Zeeman shift is calculated from the shift coefficient from [57] and the splitting $\Delta\nu_{\pm 9/2}$ between the two m_F clock transitions, which is tracked during the clock stabilisation. During measurements of the lattice light shift we have seen that this splitting contains only a negligible contribution from a vector light shift of less than 10 mHz. At our typical Zeeman splitting of about 540 Hz and daily variations of less than 0.3 Hz, the uncertainty of the second-order Zeeman shift amounts to 2.8×10^{-19}. As this is one order of magnitude below the total clock uncertainty, for simplicity we do not apply time-resolved Zeeman shift corrections.

4.4. Background gas collisions

The fractional frequency shift of strontium due to collisions with room temperature H_2 molecules, which usually dominate in ultra-high vacuum systems, can be calculated by $\Delta\nu_{\mathrm{HC}}/\nu_0 = -30(3)\times 10^{-18}\,\mathrm{s}/\tau_{\mathrm{trap}}$ [58]. In the BBR shield, we measure $1/e$ lifetimes of lattice-trapped $^1\mathrm{S}_0$ atoms ranging from 9 s to 15 s, while at the MOT position we measure lifetimes of magnetically trapped $^3\mathrm{P}_2$ atoms of up to 22 s. Due to possible additional loss mechanisms, the measured lattice trap lifetimes only represent a lower bound for the collision-limited trap lifetime. We estimate the background gas collision shift to be in the middle between the H_2 collision values associated with the two extreme measured lifetimes (9 s and 22 s), and the uncertainty such that both values are covered, that is $-2.3(1.0)\times 10^{-18}$.

4.5. Other contributions

The clock laser light shift is given by $\Delta\nu_p/\nu_0 = \chi I$, with the light shift at the clock transition of about $\chi = -26\ \mathrm{Hz\ cm^2\ W^{-1}}$ [44] and the beam intensity $I = \frac{11}{9}\frac{2\pi^3 h\nu_0^3 \tau_{^3\mathrm{P}_0}}{3c^2\tau_p^2}$ for the Rabi π pulse duration τ_p, with the Planck constant h, the speed of light c, and the upper state lifetime $\tau_{^3\mathrm{P}_0} = 118(3)\,\mathrm{s}$ [59]. For $\tau_p = 500\,\mathrm{ms}$ we find a negligible light shift of -4.2×10^{-20}, which is also considered as its uncertainty. Due to the conservative estimate the influence of the Lamb-Dicke parameter on the Rabi frequency is neglected, as it only increases the probe light shift by less than 20%. Also the differing atomic lifetime recently measured in [60] only causes a shift difference well within the given uncertainty.

The possible size of a DC Stark shift is estimated from the shifts observed near the hole edges discussed in section 3, i.e. $-1(1)\times 10^{-19}$, where the uncertainty is estimated to be equal to the magnitude. Generally, the coating's low surface resistivity of $\leqslant 2\times 10^6\ \Omega/\square$ [61] counters charge accumulation on the walls. No electric fields from patch charges or small coating variations on the inner BBR shield walls are expected to be noticeable as the walls further have a minimum distance to the atoms of 5 mm. Electric fields from the outside are well shielded by the BBR copper shield.

A temporal change of the clock laser cavity drift leads to a servo error when the servo adjusting the feed forward for drift compensation cannot follow fast enough [41]. For typical operation conditions of our clock, we arrive at a servo error of $0(2)\times 10^{-19}$.

Line pulling by transitions starting from $m_F \neq \pm 9/2$ is heavily suppressed by the removal of populations from these levels during state preparation. Excitation by $\sigma^{\pm}$ light is suppressed by the use of high quality polarisers in the clock laser beam and proper alignment with respect to the magnetic bias field. We estimate line pulling effects on the clock transition to be below 1×10^{-19}.

The linear Zeeman shift is cancelled by averaging the frequencies of the two $|^3\mathrm{P}_0, m_F = \pm\frac{9}{2}\rangle \rightarrow |^1\mathrm{S}_0, m_F = \pm\frac{9}{2}\rangle$ clock transitions. However, a slowly fluctuating Zeeman splitting between these two transitions can result in a lock error. With a maximum observed drift per day of $\Delta\dot{\nu}_{\pm 9/2} = 0.2\,\mathrm{Hz/d}$

Table 1. Values and uncertainties for various frequency shifts in the transportable clock, for $T_{\text{shield}} = -100.18(2)\,^\circ$C.

Frequency shift	Value (10^{-18})	Unc. (10^{-18})
BBR from T_{shield}	–560.2	0.3
BBR from T_{out}	–5.6	0.3
Density	+0.1	0.4
Lattice light	+7.4	1.7
Second-order Zeeman	–170.3	0.3
Background gas collision	–2.3	1.0
Clock light	–0.04	0.04
DC Stark	–0.1	0.1
Servo error	0.0	0.2
Minor shifts	0.0	<0.1
Total	–730.9	2.1

and a typical cycle time $t_{\text{seq}} = 1.6$ s, we estimate a maximum lock offset of $\Delta\dot{\nu}_{\pm 9/2} \cdot t_{\text{seq}}/2\nu_0 = 4 \times 10^{-21}$ for our interrogation sequence, which is negligible.

4.6. Total systematic uncertainty and height reference

Values and uncertainties of the systematic shifts of the transportable clock are given in table 1. The total estimated systematic uncertainty of the clock is 2.1×10^{-18}.

Applications that depend on the uncertainty budget such as clock comparisons also require correcting for differences in relativistic redshift. This can be achieved by measuring the vertical height differences of the atomic samples with respect to external height reference markers. The differential relativistic redshift is then determined using the local gravity acceleration, which is required to connect each clock's geopotential value to that of the respective reference marker, and the geopotential difference between markers. This effect is usually treated separately from the clocks' other systematic effects. In our case, the vertical height difference with respect to a reference marker next to the physics package is known with an uncertainty of 1 mm, which leads to a negligible additional fractional uncertainty contribution of about 1×10^{-19}.

5. Absolute frequency measurement

The frequency of the transportable clock Sr4 was determined by comparison to the primary caesium fountain clocks CSF1 and CSF2 at PTB [32] as described in [62]: the frequency of Sr4 is measured on shorter, interrupted intervals relative to a continuously running maser that serves as flywheel. The average maser frequency on a longer, continuous interval is measured by the fountain clocks. Combining both measurements and correcting for the differential gravitational redshift between the clocks provides the absolute frequencies reported in table 2. The centres of gravity of each clock's measurement versus the maser are adjusted to be the same such that the result is insensitive to a linear drift of the maser frequency in time. Due to the noise of the flywheel oscillator's frequency, the average frequency measured by the strontium and caesium clocks may differ. The related extrapolation uncertainty u_{ext} is estimated using a sensitivity function based on the measurement intervals and a noise model of the flywheel [62, 63]. We have verified the previously observed noise assumptions on the hydrogen maser by comparisons with our optical clocks and find as the only deviation a reduced frequency flicker floor of 1×10^{-16} (see appendix E for details).

We include an additional uncertainty u_{RF} for the RF cables and the RF synthesis at the comb [64]. It has been estimated by comparing simultaneous absolute frequency measurements of the same optical reference at two separate optical frequency combs with independent RF cables and RF synthesis chains linking the 100 MHz reference from the maser to the comb repetition rates. For these tests, a common optical reference was provided to the combs via end-to-end stabilised fibres, resulting in an uncertainty arising from the optical comb and fibre links below 10^{-20} as shown in [35].

We treat the systematic corrections of each clock as correlated between measurements but not between different clocks, the extrapolation errors and the RF link and synthesis errors as correlated between measurements using the same time interval, and all other effects as uncorrelated. Average results for each fountain clock and overall have been computed with weights that have been optimised by a least-squares algorithm to yield the lowest uncertainty including correlations (see appendix F for details).

We find average frequencies of the ${}^1\text{S}_0 \rightarrow {}^3\text{P}_0$ clock transition in ^{87}Sr of 429 228 004 229 872.801(201) Hz using CSF1 and 429 228 004 229 872.975(86) Hz using CSF2, which are mostly limited by the systematic

Table 2. Summary of the relevant information on the absolute frequency measurements for the respective measurement intervals labelled by the Modified Julian Date (MJD, centre of gravity). $\Delta\nu$ is the value to be added to 429 228 004 229 000 Hz to get the frequency ν_{Sr} of the $5s^2\,{}^1S_0 \rightarrow 5s5p\,{}^3P_0$ transition in ^{87}Sr measured by the fountain clocks CSF1 and CSF2, respectively. The statistical uncertainty contribution from the Sr frequency standard is below 7×10^{-18} for each measurement and therefore negligible.

					CSF1					CSF2				
MJD	T_{Sr} (s)	$u_{b,\mathrm{Sr}}$ (10^{-18})	u_{ext} (10^{-16})	u_{RF}	T_{Cs} (days)	$u_{a,\mathrm{Cs}}$ (10^{-16})	$u_{b,\mathrm{Cs}}$	$\Delta\nu$ (Hz)	u (Hz)	T_{Cs} (days)	$u_{a,\mathrm{Cs}}$ (10^{-16})	$u_{b,\mathrm{Cs}}$	$\Delta\nu$ (Hz)	u (Hz)
60 055	27 604	17.0	1.6	0.3	2.52	8.2	2.8	872.79	0.38	2.52	3.3	1.7	873.11	0.17
60 060	108 898	15.0	0.8	0.3	3.82	6.7	3.2	872.80	0.32	3.82	2.7	1.7	872.95	0.14
60 368	7679	3.5	3.0	0.3	2.09	9.3	4.7	872.36	0.47	2.09	3.8	1.7	872.75	0.22
60 371	78 470	4.2	1.0	0.3	3.07	7.8	5.6	873.00	0.41	3.07	3.2	1.7	873.05	0.16
60 374	79 960	5.1	0.9	0.3	3.63	7.1	5.4	872.99	0.39	3.63	3.3	1.7	873.04	0.16
60 385	69 140	5.2	1.1	0.3	2.86	8.1	5.0	872.80	0.41	2.86	4.5	1.7	872.71	0.21
60 580	66 629	8.5	1.1	0.3						3.16	3.1	1.7	873.06	0.16
60 592	157 385	7.7	0.6	0.3						4.37	2.7	1.7	873.05	0.14
60 720	129 451	2.4	0.8	0.3	3.50	7.3	1.9	872.82	0.33	3.50	3.0	1.7	872.83	0.15
60 725	225 037	2.4	0.5	0.3						4.33	3.5	1.7	872.98	0.17
Average								872.801	0.201				872.975	0.086

uncertainties of fountain clocks. The overall average frequency 429 228 004 229 872.951(80) Hz has a fractional uncertainty of 1.9×10^{-16} and is in agreement with previous measurements [65]. Relevant correlation coefficients are reported in appendix F.

6. Summary and outlook

We have described a transportable strontium lattice clock with a BBR shift uncertainty of 4.0×10^{-19}, getting the BBR shift under better control compared to state-of-the-art lab-based strontium lattice clocks, where it often represents the largest systematic uncertainty contribution. This was achieved by interrogating the atoms in a thermal shield with low homogeneous temperature and carefully characterised apertures to the outside. The low self-comparison instability of $7 \times 10^{-16}/\sqrt{\tau/\mathrm{s}}$ using the transportable clock laser [30] allows quick recharacterisations of systematic effects. This enables a total systematic uncertainty of 2.1×10^{-18}, both on- and off-campus, that is comparable to the current relativistic redshift uncertainty at the geodetically best-surveyed locations, using state-of-the-art geodetic techniques [13], or even below that [66–68]. Furthermore, by comparing the clock to the caesium fountains CSF1 and CSF2 at PTB, we have measured the frequency of the ${}^1S_0 \rightarrow {}^3P_0$ clock transition of ^{87}Sr.

In [11] the first measurement campaign of this clock is presented. Throughout following measurement campaigns, the uncertainty as well as the stability of the clock could be improved to reach the clock performance presented here. It is planned to participate in inter-institute frequency comparisons at the 10^{-18} level. This transportable clock is therefore expected to facilitate the development of cm-level chronometric geodesy [12, 69, 70]. A further improvement of the clock's uncertainty and reproducibility appears to be feasible by extended investigations of the lattice light shift [56] and the density shift [71].

Data availability statement

The data that support the findings of this study are openly available at the following URL/DOI: https://doi.org/10.7795/720.20250926.

Acknowledgments

We thank Richard Hobson for help in designing the pyramid MOT. Regarding the construction of the pyramid MOT mirrors, we thank André Uhde and Mandy Rindermann for manufacturing the copper substrates, Rudolf Meeß and Stefan Verhülsdonk for the surface processing of their optical surfaces, and Daniel Hagedorn and Steffen Weiß for applying their coatings. We also express our gratitude to André Uhde for machining the BBR shield, and to Michael Neugebauer, Daniel Bennett, Erik Jansson and Elena Jordan for helping in the characterisation of its hole radii. We thank Kilian Stahl and Joshua Klose for operating the laboratory clock Sr3 as a stable reference, and Uwe Sterr and Thomas Legero for providing it with ultrastable laser light.

We acknowledge support by the Deutsche Forschungsgemeinschaft (DFG, German Research Foundation) under Germany's Excellence Strategy—EXC-2123 QuantumFrontiers—Project-ID

3908379.67 and SFB 1464 TerraQ—Project-ID 434617780—within project A04. This work was partially supported by the Max Planck-RIKEN-PTB Center for Time, Constants and Fundamental Symmetries. This work has received funding from the European Partnership on Metrology, co-financed by the European Union's Horizon Europe Research and Innovation Programme and by the Participating States, under Grant number 22IEM01 TOCK.

Author contributions

I N, C V, T L, and C L designed the transportable clock including the BBR shield. I N, C V, and T L built, operated and characterised the transportable clock. J R, N P, and S W operated the caesium fountain clocks, and E B operated a frequency comb connecting them to the transportable clock. C L, S D, and S W analysed the absolute frequency measurement results. I N, C V, T L, S D, and C L wrote the manuscript. All authors discussed the results.

Appendix A. Level scheme

A level scheme for the addressed electronic transitions described in this manuscript is shown in figure A1.

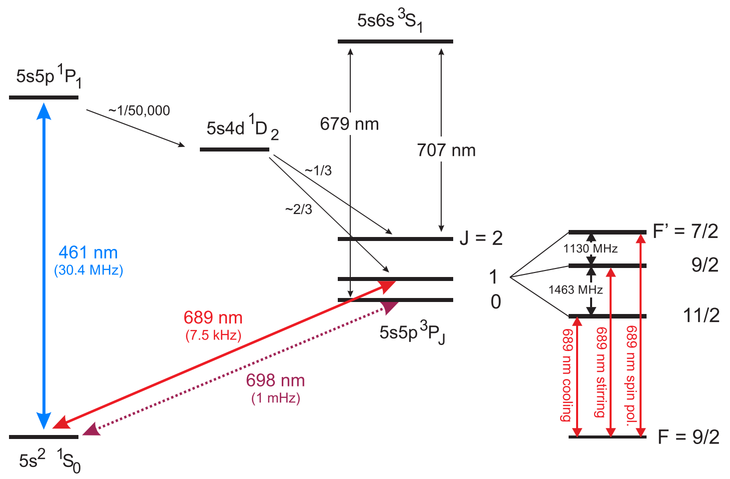

Figure A1. Partial electronic level scheme of ^{87}Sr. Linewidths for electronic transitions from the ground state are calculated from the upper state lifetimes for the $^1P_1$ [72], $^3P_1$ [6] and $^3P_0$ [59] states. Additionally shown are partial decay rates to [73] and from [74] the $^1D_2$ state, and the hyperfine splittings of the $^3P_1$ state [75].

Appendix B. BBR shield bore radii

In the estimation of the influence of external BBR on atoms in the shield, the determination of the solid angle Ω under which the atoms see the BBR shield holes, is critical. Here the radii of the bores are the parameters the most difficult to determine. The radii of the holes were measured using a coordinate measuring machine (CMM) with a ruby ball stylus with diameter 300 μm before the inner surfaces were coated. The positions of 16 points on each of three planes at depths of 100 μm, 500 μm and 900 μm have been measured for each hole, from which the radius at each depth was determined. It was found that the hole radii shrink by about 8 μm towards the inside. As the radii at the outer hole edges are relevant for determining the frequency shift of the atoms due to room temperature BBR, we linearly extrapolated to the outer edge. We find radii $r^{\text{out}}_{\text{CMM},1} = 0.5205(15)\,\text{mm}$ and $r^{\text{out}}_{\text{CMM},2} = 0.5225(15)\,\text{mm}$.

Additionally, we measured the radii along eight orientations for each hole by a measuring microscope (MM) before and after applying the black coating on the inner hole surfaces and cold-welding the shield lid onto the main body of the shield, $r^{\text{before}}_{\text{MM},i}(\alpha)$ and $r^{\text{after}}_{\text{MM},i}(\alpha)$. Due to the coating and an emerging slight ellipticity of the holes due to the pressing of the top lid on the main body, we observed a reduction of radii with respect to the average bore radii determined with the measurement microscope before. While using the measurement microscope has the advantage of enabling non-tactile measurements which do not damage the coating, it provides less accurate results for deep holes. This data are corrected by the

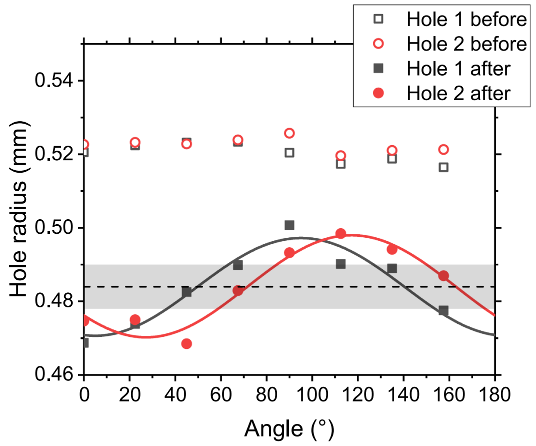

Figure B1. The radii of the two holes of the BBR shield plotted over the angle between the axis towards the BBR shield top lid and the direction of measurement. They are shown both before and after the black coating and the connection of the two BBR shield parts. The latter are fitted with the formula for the angle-dependent radius of an ellipse $r(\alpha) = \left(\left[r_{\min}\cos\left(\pi\,\frac{\alpha-\alpha_0}{180^\circ}\right)\right]^2 + \left[r_{\max}\sin\left(\pi\,\frac{\alpha-\alpha_0}{180^\circ}\right)\right]^2\right)^{1/2}$. The solid lines show the respective fit results, and the dashed line the effective radius r_{eff} with its uncertainty (grey area).

Table B1. Uncertainty contributions of the fractional solid angle of the two BBR shield holes.

Quantity	Value	Uncertainty	$\delta(\Omega/4\pi)$
Hole radii r_1 and r_2	484 μm (both)	6 μm (both)	2.5×10^{-5}
Atom position z	0 mm	0.5 mm	0.9×10^{-5}
BBR shield length ℓ	20 mm	0.1 mm	1.2×10^{-5}
			Total: 2.9×10^{-5}

difference between the CMM results and the initial average measurement microscope results, $\Delta r_{\mathrm{CMM},i} = r^{\mathrm{out}}_{\mathrm{CMM},i} - \overline{r^{\mathrm{before}}_{\mathrm{MM},i}}$, which corresponds to $+3.5\,\mu$m for hole 1 and $+6.5\,\mu$m for hole 2.

The resulting data are shown in figure B1. The effective radius for the holes after coating and connection is calculated by $r_{\mathrm{eff},i} = (r_{\min,i}\,r_{\max,i})^{1/2}$, with the fitted minimum and maximum radii $r_{\min,i}$ and $r_{\max,i}$. We find for both bores $r_{\mathrm{eff}} = 0.484(6)$ mm, with the uncertainty mostly stemming from the measurements with the measurement microscope.

The uncertainty of the offset of the atoms from the centre of the BBR shield is estimated to be 0.5 mm. This is based on the measurement of the BBR shield hole positions shown in figure 4(a). The uncertainty of the BBR shield length is estimated to be 0.1 mm. Close to the centre of the BBR shield, where $|z|, r_1, r_2 \ll \frac{\ell}{2}$, (2) simplifies to

$$\frac{\Omega}{4\pi} \approx \frac{r_1^2}{4\left(z+\frac{\ell}{2}\right)^2} + \frac{r_2^2}{4\left(z-\frac{\ell}{2}\right)^2}\,, \tag{B1}$$

from which we calculate the uncertainty contributions in table B1.

We note that the radii shrink by up to 0.3% if the copper shield is cooled from room temperature to cryogenic temperatures [76], i.e. by up to 1.5 μm—however, as also the length of the BBR shield shrinks in the same way, the Ω stays constant to a good approximation.

Appendix C. Emissivity of the BBR shield coating

On the inner surfaces of the BBR shield the high-emissivity coating Ultra Black$^{\mathrm{TM}}$ by Acktar is applied. Based on the hemispherical reflectance in the wavelength range 2.6 ... 17 μm certified by the supplier, the average emissivity of our coating in that range is calculated to be $\epsilon_{\mathrm{cert}} = 0.926(7)$. Similar emissivity values above 0.9 have been reported for this coating type for larger wavelengths [77, 78] and up to 50 μm [79]. As at room temperature only 3.2% ($< 0.001\%$) of the total BBR spectral radiance, $B_\lambda(T) = \frac{2hc^2}{\lambda^5}\frac{1}{e^{hc/(k_B T\lambda)}-1}$, is in the wavelength range $\lambda > 50\,\mu$m ($\lambda < 2.6\,\mu$m), we consider the previously stated value to be a good approximation for the average emissivity across the entire BBR spectrum. We assume a rectangular probability distribution of the true emissivity value in the range

$\epsilon_{\text{in}} = \epsilon_{\text{cert}} \pm (1 - \epsilon_{\text{cert}})$ [50], which is chosen relatively large in order to account for uncertainties arising from, e.g. the missing knowledge of the exact wavelength and angle dependence of the emissivity, and arrive at $\epsilon_{\text{in}} = 0.926(43)$.

Appendix D. Shift from hole edges at BBR shield centre

In order to determine the residual frequency shift that electric charges at the inner edges of the BBR shield's holes cause in atoms at the centre of the shield ($z = 0$), we use a fit function proportional to the squared electric field resulting from a ring of charge with radius r (expected to be 0.48 mm) at position $z = z_r$, i.e.

$$\Delta\nu = -A \frac{r^2 \left(z - z_r\right)^2}{\left(\left(z - z_r\right)^2 + r^2\right)^{y/2+1}} \, . \tag{D1}$$

In the case of $|z - z_r| \gg r$, this function corresponds to $\Delta\nu = -A\frac{r^2}{(z-z_r)^y}$. For an unshielded ring of charge (as well as for a point charge), $y = 4$ is expected, while the FEM simulation of the hole edge frequency shifts outlined in section 3 suggests an even more rapid falling off behaviour. We fit (D1) to the frequency shifts observed near the inner edge of each hole, allowing the parameters A, z_r, and either y or r to vary, while we fix the remaining parameter (r or y) to its expected value. For the upper hole [lower hole] we find $y = 7.5$ [3.7] and $r = 0.29$ mm [0.53 mm]. In both cases, the combined residual shift from both holes at the BBR shield centre is -1×10^{-19} or less.

Appendix E. Maser noise model

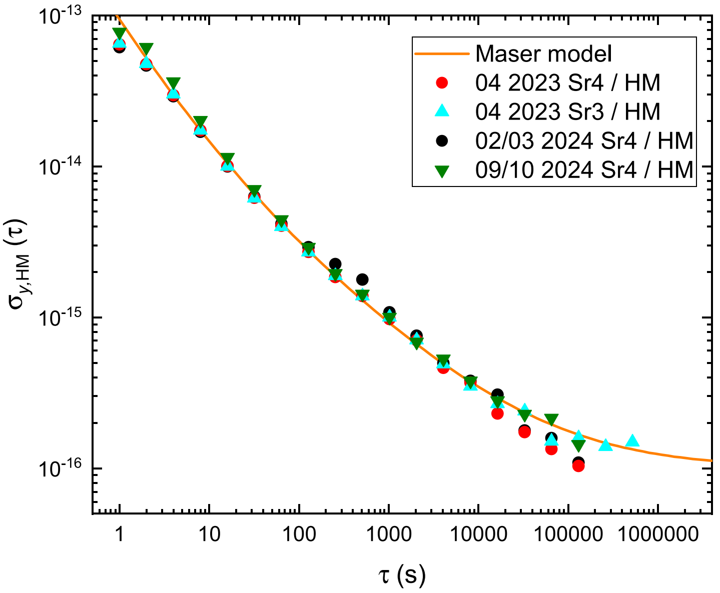

Figure E1. Allan deviations showing the hydrogen maser's frequency stability as measured by Sr lattice clocks at PTB. The curve depicts the maser instability derived from the maser noise model.

For the measurement intervals listed in table 2, we have modelled the noise spectrum of the hydrogen maser that was used as flywheel oscillator by the power law expansion $S_y = \sum_{\alpha=-1}^{1} h_\alpha f^\alpha$ of the single-sided power spectral density $S_y(f)$ by adding flicker frequency (FFN), white frequency (WFN) and flicker phase noise (FPN) contributions. The coefficients h_α are adjusted such that the calculated Allan deviation $\sigma_{y,\text{HM}}$ [80, 81] matches the observations in figure E1. We find the coefficients

$$\begin{aligned} h_1 = 4.3\times10^{-26}\,\mathrm{Hz}^{-2} \quad &\Rightarrow \quad \sigma_{y,\mathrm{FPN}} = 7\times10^{-14}\,\mathrm{s}/\tau \\ h_0 = 1.2\times10^{-27}\,\mathrm{Hz}^{-1} \quad &\Rightarrow \quad \sigma_{y,\mathrm{WFN}} = 2.4\times10^{-14}\,\sqrt{\mathrm{s}/\tau} \\ h_{-1} = 7.2\times10^{-33} \quad &\Rightarrow \quad \sigma_{y,\mathrm{FFN}} = 1\times10^{-16} \end{aligned} \tag{E1}$$

using a cut-off frequency of 0.5 Hz.

Appendix F. Correlation analysis and averaging of absolute frequency measurements

The evaluation of the weighted average values reported for the absolute frequency in section 5 (see also table 2) takes into account the correlations between the measurements. We follow the general notation introduced in [82]. To facilitate comparisons to other results, we analyse the correlations of the measurements to specific error contributions, Δ_k, i.e. the random variables underlying uncertainty contributions u_k, such as the systematic uncertainties of the clocks. These error contributions are—exactly or approximately—either fully correlated or uncorrelated between measurements: the systematic errors of each clock are treated as fully correlated between measurements but uncorrelated between clocks; the extrapolation errors as well as the RF link and synthesis errors are fully correlated between all measurements within the same interval and treated as uncorrelated otherwise; the fountain clocks' statistical errors are uncorrelated; we neglect the statistical error of the optical clock, which can be considered part of the extrapolation error. The covariance $u(\nu_i, \Delta_k)$ between a measurement ν_i and a relative error Δ_k is then given by the respective uncertainty contribution listed in table 2 or zero. We note that the covariances are negative for the systematic errors of the fountain clocks as the frequency measured for the optical clock decreases if their frequency is increased.

Given a set of weights w_i where $\sum_i w_i = 1$, the weighted average value and its covariances with respect to the independent quantities Δ_k are then given by:

$$\bar{\nu} = \sum_{i=1}^{N} w_i \nu_i \tag{F1}$$

$$u(\bar{\nu}, \Delta_k) = \sum_{i=1}^{N} w_i\, u(\nu_i, \Delta_k)\,. \tag{F2}$$

The uncertainty is

$$u(\bar{\nu}) = \sqrt{\sum_{k=1}^{K} u(\bar{\nu}, \Delta_k)^2} \tag{F3}$$

since the Δ_k account for all relevant independent quantities. Finally, the correlation coefficients between two quantities, q_i and q_j, can readily be derived using [82]

$$r(q_i, q_j) = \frac{u(q_i, q_j)}{u(q_i)\,u(q_j)}, \tag{F4}$$

where the uncertainty of the relative errors $u(\Delta_k)$ is one.

We determine optimised sets of weights w_i for the full data set as well as the subsets measured against a specific fountain by minimising the uncertainty $u(\bar{\nu})$ using a least-squares algorithm with equal weights as initial estimate. The weights are summarised in table F1. For comparison, we also include the weights that would result from simply using the combined statistical, extrapolation, and RF link and synthesis variances ($w_i' \propto 1/(u_\mathrm{a}^2 + u_\mathrm{ext}^2 + u_\mathrm{RF}^2)$) for the CSF1 and CSF2 subsets. The optimised weights reproduce the fixed weights well for the CSF2 subset, which is expected because the systematic uncertainty of the fountain is nearly constant across the measurements. The other fountain clock's systematic uncertainty by contrast varies substantially between measurements. The optimised set thus assigns higher weights to the more accurate measurements in this case in comparison to the fixed weights, which leads to a moderate reduction of the uncertainty (by about 6%).

Concerning the uncertainty of the overall average, we note that both the increase by including the correlations between the subset averages that arise from extrapolation errors (<1%) as compared to the weighted average used in [62] and the reduction by adopting the optimised weights (about 1%) are marginal. We report the relevant correlation coefficients in table F2.

Table F1. Weights of measurement results in the absolute frequency averages for the full data set and for the CSF1 and CSF2 subsets. In addition to the optimised weights, the weights resulting from simple weighting strategies are given for comparison; see the main text for details.

	Weight							
	CSF1 average		CSF2 average		CSF1+CSF2 average			
	simple	optimised	simple	optimised	simple		optimised	
MJD	(CSF1)	(CSF1)	(CSF2)	(CSF2)	(CSF1)	(CSF2)	(CSF1)	(CSF2)
60 055	0.123	0.181	0.085	0.085	0.015	0.075	0.026	0.068
60 060	0.189	0.248	0.145	0.144	0.022	0.127	0.038	0.121
60 368	0.090	0.067	0.049	0.049	0.011	0.043	0.008	0.039
60 371	0.140	0.055	0.102	0.103	0.017	0.090	0.009	0.088
60 374	0.168	0.079	0.098	0.098	0.020	0.086	0.013	0.084
60 385	0.129	0.081	0.054	0.054	0.015	0.047	0.013	0.046
60 580			0.107	0.107		0.094		0.093
60 592			0.149	0.149		0.131		0.129
60 720	0.160	0.290	0.120	0.120	0.019	0.106	0.045	0.101
60 725			0.092	0.093		0.081		0.080

Table F2. Correlation coefficients r of the average transition frequencies of the full data set, $\bar{\nu}(\mathrm{Sr})$, and the subsets using the same fountain clock, $\bar{\nu}(\mathrm{Sr}|i)$, with respect to each other and to the atomic clocks' systematic relative errors, $\Delta_{\mathrm{b},j}$.

q_i	q_j	$r(q_i, q_j)$
$\bar{\nu}(\mathrm{Sr}\|\mathrm{CSF1})$	$\Delta_{\mathrm{b,Sr}}$	0.019
$\bar{\nu}(\mathrm{Sr}\|\mathrm{CSF1})$	$\Delta_{\mathrm{b,CSF1}}$	−0.706
$\bar{\nu}(\mathrm{Sr}\|\mathrm{CSF2})$	$\Delta_{\mathrm{b,Sr}}$	0.037
$\bar{\nu}(\mathrm{Sr}\|\mathrm{CSF2})$	$\Delta_{\mathrm{b,CSF2}}$	−0.844
$\bar{\nu}(\mathrm{Sr})$	$\Delta_{\mathrm{b,Sr}}$	0.041
$\bar{\nu}(\mathrm{Sr})$	$\Delta_{\mathrm{b,CSF1}}$	−0.270
$\bar{\nu}(\mathrm{Sr})$	$\Delta_{\mathrm{b,CSF2}}$	−0.775
$\bar{\nu}(\mathrm{Sr})$	$\bar{\nu}(\mathrm{Sr}\|\mathrm{CSF1})$	0.397
$\bar{\nu}(\mathrm{Sr})$	$\bar{\nu}(\mathrm{Sr}\|\mathrm{CSF2})$	0.924

ORCID iDs

I Nosske 0000-0003-3622-4527
C Vishwakarma 0000-0001-5343-9832
T Lücke 0009-0001-3007-1761
J Rahm 0000-0002-4832-8043
N Poudel 0000-0002-5929-6235
S Weyers 0000-0003-4484-6481
E Benkler 0000-0001-7907-849X
S Dörscher 0000-0002-3331-4001
C Lisdat 0000-0002-4705-8854

References

[1] Huntemann N, Sanner C, Lipphardt B, Tamm C and Peik E 2016 *Phys. Rev. Lett.* **116** 063001
[2] McGrew W F *et al* 2018 *Nature* **564** 87–90
[3] Brewer S M, Chen J S, Hankin A M, Clements E R, Chou C W, Wineland D J, Hume D B and Leibrandt D R 2019 *Phys. Rev. Lett.* **123** 033201
[4] Huang Y, Zhang B, Zeng M, Hao Y, Ma Z, Zhang H, Guan H, Chen Z, Wang M and Gao K 2022 *Phys. Rev. Appl.* **17** 034041
[5] Tofful A *et al* 2024 *Metrologia* **61** 045001
[6] Aeppli A, Kim K, Warfield W, Safronova M S and Ye J 2024 *Phys. Rev. Lett.* **133** 023401
[7] Arnold K J, Bustabad S, Qi Z, Qichen Q, Zhang Z, Zhao Z and Barrett M D 2024 Validating a lutetium frequency reference *J. Phys.: Conf. Ser.* **2889** 012040
[8] Hausser H N *et al* 2025 *Phys. Rev. Lett.* **134** 023201
[9] Lu X T, Guo F, Liu Y Y, Cao J, Li J A, Xia J J, Xu Q F, Lu B Q, Wang Y B and Chang H 2025 *Metrologia* **62** 035007
[10] Dimarcq N *et al* 2024 *Metrologia* **61** 012001
[11] Amy-Klein A *et al* (ICON: International Clock and Oscillator Networking Collaboration) 2024 International comparison of optical frequencies with transportable optical lattice clocks (arXiv:2410.22973[physics.atom-ph])
[12] Mehlstäubler T, Grosche G, Lisdat C, Schmidt P and Denker H 2018 *Rep. Prog. Phys.* **81** 064401
[13] Denker H, Timmen L, Voigt C, Weyers S, Peik E, Margolis H S, Delva P, Wolf P and Petit G 2018 *J. Geod.* **5** 487–516

[14] Koller S B, Grotti J, Vogt S, Al-Masoudi A, Dörscher S, Häfner S, Sterr U and Lisdat C 2017 *Phys. Rev. Lett.* **118** 073601

[15] Origlia S *et al* 2018 *Phys. Rev. A* **98** 053443

[16] Huang Y *et al* 2020 *Phys. Rev. A* **102** 050802

[17] Ohmae N *et al* 2021 *Adv. Quantum Technol.* **4** 2100015

[18] Stuhler J *et al* 2021 *Meas.: Sens.* **18** 100264

[19] Guo F *et al* 2021 *AIP Adv.* **11** 125116

[20] Kale Y B, Singh A, Gellesch M, Jones J M, Morris D, Aldous M, Bongs K and Singh Y 2022 *Quantum Sci. Technol.* **7** 045004

[21] Liu D X, Cao J, Yuan J B, Cui K F, Yuan Y, Zhang P, Chao S J, Shu H L and Huang X R 2023 *Chin. Phys. B* **32** 010601

[22] Zeng M *et al* 2023 *Phys. Rev. Appl.* **19** 064004

[23] Brand W 2024 A transportable ytterbium optical lattice clock with eighteen digits of accuracy *PhD Thesis* University of Colorado at Boulder

[24] Hobson R, Bowden W, William A, Silva A, Baynham C F A, Margolis H S, Baird P E G, Gill P and Hill I R 2020 *Metrologia* **57** 065026

[25] Goti I, Condio S, Clivati C, Risaro M, Gozzelino M, Costanzo G A, Levi F, Calonico D and Pizzocaro M 2023 *Metrologia* **60** 035002

[26] Li J *et al* 2024 *Metrologia* **61** 015006

[27] Ushijima I, Takamoto M, Das M, Ohkubo T and Katori H 2015 *Nat. Photon.* **9** 185–9

[28] Yu H, Liu P, Li Y, Jia Z, Zhang X, Yan J, Li J, Dai H and Chen Y 2025 *Measurement* **15** 118527

[29] Hassan Y S *et al* 2025 *Phys. Rev. Lett.* **135** 063402

[30] Herbers S, Häfner S, Dörscher S, Lücke T, Sterr U and Lisdat C 2022 *Opt. Lett.* **47** 5441–4

[31] Häfner S, Herbers S, Vogt S, Lisdat C and Sterr U 2020 *Opt. Express* **28** 16407–16

[32] Weyers S, Gerginov V, Kazda M, Rahm J, Lipphardt B, Dobrev G and Gibble K 2018 *Metrologia* **55** 789–805

[33] Schioppo M *et al* 2022 *Nat. Commun.* **13** 212

[34] Clivati C *et al* 2020 *Optica* **7** 1031–7

[35] Benkler E, Lipphardt B, Puppe T, Wilk R, Rohde F and Sterr U 2019 *Opt. Express* **27** 36886–902

[36] Hill I R, Ovchinnikov Y B, Bridge E M, Curtis E A and Gill P 2014 *J. Phys. B: At. Mol. Phys.* **47** 075006

[37] Bowden W, Hobson R, Hill I R, Vianello A, Schioppo M, Silva A, Margolis H S, Baird P E G and Gill P 2019 *Sci. Rep.* **9** 11704

[38] Mukaiyama T, Katori H, Ido T, Li Y and Kuwata-Gonokami M 2003 *Phys. Rev. Lett.* **90** 113002

[39] Schwarz R 2022 A cryogenic strontium lattice clock *PhD Thesis* Gottfried Wilhelm Leibniz Universität Hannover

[40] Matei D G *et al* 2017 *Phys. Rev. Lett.* **118** 263202

[41] Falke S *et al* 2011 *Metrologia* **48** 399–407

[42] Al-Masoudi A, Dörscher S, Häfner S, Sterr U and Lisdat C 2015 *Phys. Rev. A* **92** 063814

[43] Middelmann T, Falke S, Lisdat C and Sterr U 2012 *Phys. Rev. Lett.* **109** 263004

[44] Lisdat C, Dörscher S, Nosske I and Sterr U 2021 *Phys. Rev. Res.* **3** L042036

[45] Kim K, Aeppli A and Ye J 2025 private communication

[46] Porsev S G and Derevianko A 2006 *Phys. Rev. A* **74** 020502(R)

[47] Tang Z M, Wei Y F, Sahoo B K, Li C B, Yang Y, Zou Y and Huang X R 2024 *Phys. Rev. A* **110** 043108

[48] Middelmann T, Lisdat C, Falke S, Vellore Winfred J S R, Riehle F and Sterr U 2011 *IEEE Trans. Instrum. Meas.* **60** 2550–7

[49] Abdel-Hafiz M *et al* 2019 Guidelines for developing optical clocks with 10^{-18} fractional frequency uncertainty (arXiv:1906.11495[physics.atom-ph])

[50] Evaluation of measurement data – guide to the expression of uncertainty in measurement JCGM 100:2008 2008 (available at: http://www.bipm.org/utils/common/documents/jcgm/JCGM_100_2008_E.pdf)

[51] Gaiser C *et al* 2022 *J. Phys. Chem. Ref. Data* **51** 043105

[52] Dick G J 1989 Local oscillator induced instabilities in trapped ion frequency standards *Proc. of 19th Annu. Precise Time and Time Interval Meeting, Redondo Beach, 1987 ADA502386* (U.S. Naval Observatory) pp 133–47 (available at: www.ion.org/publications/abstract.cfm?articleID=15462)

[53] Swallows M, Martin M, Bishof M, Benko C, Lin Y, Blatt S, Rey A and Ye J 2012 *IEEE Trans. Ultrason. Ferroelectr. Freq. Control* **59** 416–25

[54] Ushijima I, Takamoto M and Katori H 2018 *Phys. Rev. Lett.* **121** 263202

[55] Brown R C *et al* 2017 *Phys. Rev. Lett.* **119** 253001

[56] Kim K, Aeppli A, Bothwell T and Ye J 2023 *Phys. Rev. Lett.* **130** 113203

[57] Bothwell T, Kedar D, Oelker E, Robinson J M, Bromley S L, Tew W L, Ye J and Kennedy C J 2019 *Metrologia* **56** 065004

[58] Alves B X R, Foucault Y, Vallet G and Lodewyck J 2019 Background gas collision frequency shift on lattice-trapped strontium atoms *2019 Joint Conf. IEEE Int. Frequency Control Symp. and European Frequency and Time Forum (EFTF/IFC)* (IEEE) pp 1–2

[59] Muniz J A, Young D J, Cline J R K and Thompson J K 2021 *Phys. Rev. Res.* **3** 023152

[60] Lu X T, Guo F, Liu Y Y, Xia J J, Zhao G D, Chen Y X, Wang Y B, Lu B Q and Chang H 2024 *Phys. Rev. Appl.* **21** 024042

[61] Acktar, specifications for Ultra BlackTM Coating (available at: https://acktar.com/product/ultra-black/) (Accessed 13 August 2025)

[62] Schwarz R, Dörscher S, Al-Masoudi A, Benkler E, Legero T, Sterr U, Weyers S, Rahm J, Lipphardt B and Lisdat C 2020 *Phys. Rev. Res.* **2** 033242

[63] Grebing C, Al-Masoudi A, Dörscher S, Häfner S, Gerginov V, Weyers S, Lipphardt B, Riehle F, Sterr U and Lisdat C 2016 *Optica* **3** 563–9

[64] We note that, unlike in previous publications [62, 83], conversion between the optical and microwave domains was performed mostly on a frequency comb located in a different building than the hydrogen maser and fountain clocks

[65] Margolis H S, Panfilo G, Petit G, Oates C, Ido T and Bize S 2024 *Metrologia* **61** 035005

[66] Pavlis N K and Weiss M A 2017 *Metrologia* **54** 535

[67] Grotti J *et al* 2018 *Nat. Phys.* **14** 437–41

[68] Lee J, Kwon J H, Park C Y, Kim H, Choi I M, Chung J W and Lee W K 2024 *Metrologia* **61** 015008

[69] Tanaka Y and Katori H 2021 *J. Geod.* **95** 1–14

[70] Takamoto M, Tanaka Y and Katori H 2022 *Appl. Phys. Lett.* **120** 140502

[71] Aeppli A, Chu A, Bothwell T, Kennedy C J, Kedar D, He P, Rey A M and Ye J 2022 *Sci. Adv.* **8** eadc9242

[72] Heinz A, Park A J, Šantíc N, Trautmann J, Porsev S G, Safronova M S, Bloch I and Blatt S 2020 *Phys. Rev. Lett.* **124** 203201

[73] Hunter L R, Walker W A and Weiss D S 1986 *Phys. Rev. Lett.* **56** 823–6

[74] Bauschlicher J C W, Langhoff S R and Partridge H 1985 *J. Phys. B: At. Mol. Phys.* **18** 1523–32

[75] zu Putlitz G 1963 *Z. Phys.* **175** 543–52
[76] Beenakker J J M and Swenson C A 1955 *Rev. Sci. Instrum.* **26** 1204–5
[77] Kuzmenko P J, Zeibel J G and Huynh Q 2018 Hemispherical total reflectance from 2 to 25 micron wavelength for vacuum compatible IR black coatings *Proc. SPIE* **10706** 1495–508
[78] Kononogova E, Adibekyan A, Monte C and Hollandt J 2019 *J. Sens. Sens. Syst.* **8** 233–42
[79] Acktar 2025 private communication
[80] Dawkins S T, McFerran J J and Luiten A N 2007 *IEEE Trans. Ultrason. Ferroelectr. Freq. Control* **54** 918–25
[81] Benkler E, Lisdat C and Sterr U 2015 *Metrologia* **52** 565
[82] Margolis H and Pizzocaro M 2020 Guidelines on the evaluation and reporting of correlation coefficients between frequency ratio measurements *Technical Report* 18SIB05 ROCIT (available at: http://empir.npl.co.uk/rocit/wp-content/uploads/sites/52/2021/02/ROCIT_guidelines_on_correlations.pdf)
[83] Lindvall T *et al* 2025 *Optica* **12** 843–52